

3D Printing Macroscale Engineered Materials Using Ultrasound Directed Self-Assembly and Stereolithography

John Greenhall and Bart Raeymaekers*

A manufacturing process to 3D print engineered materials comprised of a user-specified pattern of nano- or microparticles embedded in a polymer matrix material is described. The materials are printed layer-by-layer using stereolithography, and in each layer, ultrasound directed self-assembly is employed to organize a user-specified pattern of particles. This process allows manufacturing macroscale 3D materials with a user-specified microstructure consisting of particles of any material, and contrasts with existing processes, which are often limited to laboratory scale, specific materials, and/or 2D implementations. Using this manufacturing process, 3D printing of macroscale multilayer engineered materials containing a Bouligand microstructure commonly found in composite laminate and biological materials is demonstrated. Additionally, engineered materials containing a pattern of electrically conductive nickel-coated carbon fibers are fabricated, which illustrate the feasibility of 3D printing structures with embedded insulated electrical wiring. This process finds application in manufacturing of multifunctional composite materials.

1. Introduction

Engineered materials consisting of specific patterns of nano- or microparticles embedded in a matrix can exhibit unique mechanical,^[1] electrical,^[2] thermal,^[3] acoustic,^[4] and/or electromagnetic properties,^[5] which are attributed to the specific type, geometry, and spatial pattern of the embedded particles. Such materials have been designed for application in cloaking,^[4,6] sub-wavelength imaging,^[7,8] and multifunctional composite materials with tailored electrical and mechanical properties,^[9] among others. Manufacturing engineered materials consisting of patterns of nano- or microparticles embedded in a matrix material has been achieved via three categories of techniques. Subtractive techniques such as focused-ion beam milling enable fabricating features with ultrafine resolution (<100 nm). Since each feature must be individually created, the technique requires long fabrication times and, thus, limits dimensional scalability of the resulting material specimens.^[10] Additive techniques such as interference lithography, nanoimprint lithography, and microstereolithography enable rapid patterning of features in

a scalable manner (≤ 1 cm dimensions), but only work for a limited selection of materials and/or they are restricted to fabricating 2D patterns of features, thus constraining the material properties that can be tailored.^[11–13] Alternatively, directed self-assembly (DSA) enables quasi-instantaneously organizing large quantities of particles into patterns via templated,^[14,15] template-free,^[16,17] or external field-directed techniques.^[18–24] Templated DSA employs mechanical^[14] or chemical^[15] surface modification to create regions of attraction that selectively prompt particle deposition. Templates are typically limited to nano- or microscale dimensions or require complex chemical modification to facilitate compatibility between the template and particles. Conversely, template-free DSA techniques rely on capping molecules that selectively interact with each other and with particles to organize patterns.^[16] However, a limited

selection of capping molecules and particles constrains the patterns of particles that can be assembled. External field-directed techniques employ an electric,^[18,19] magnetic,^[20,21] or ultrasound field^[22–24] as a tunable virtual mask to organize particles into specific arrangements. To organize patterns of particles, electric and magnetic field techniques require conductive and ferromagnetic particles, respectively, which restrict material choice, and/or they demand ultrahigh field strength, which limits scalability.^[18–21] As such, existing manufacturing techniques are constrained by material choice, the patterns of particles or features that can be fabricated, long fabrication times, dimensional scalability, and limited control of the macroscale geometry of the material specimen.

In contrast, ultrasound DSA employs the acoustic radiation force associated with an ultrasound wave field to assemble patterns of particles with user-specified alignment and spatial arrangement, independent of their material properties^[25] and shape,^[26] without requiring ultrahigh field strength due to low attenuation of the ultrasound wave field in a low-viscosity (bulk and shear) fluid medium, thus facilitating dimensional scalability.^[27] Combining ultrasound DSA with photocuring enables organizing patterns of particles within a thin layer of liquid photopolymer resin, and subsequently photocuring to polymerize the resin and fixate the pattern of particles in place. Only simple 2D materials have been demonstrated using ultrasound DSA with photocuring based on a laser that traces the desired specimen geometry, a technique that does not enable implementing 3D material structures.^[28,29]

J. Greenhall, Prof. B. Raeymaekers
Department of Mechanical Engineering
University of Utah
Salt Lake City, UT 84112, USA
E-mail: bart.raeymaekers@utah.edu

DOI: 10.1002/admt.201700122

Thus, the objective of this paper is to demonstrate a manufacturing process that integrates ultrasound DSA with stereolithography (SLA) based on a digital light processing projector, to 3D print macroscale engineered materials layer-by-layer. This approach enables implementing complex 3D geometries with a tailored microstructure based on a user-specified pattern of particles embedded in a polymer matrix material, unrestricted by material choice.

2. Ultrasound Directed Self-Assembly/ Stereolithography Process

Figure 1 shows a schematic of the ultrasound DSA/SLA manufacturing process. An octagonal reservoir with length $L = 30.2$ mm is lined with eight ultrasound transducers around its perimeter, and contains particles dispersed in liquid photopolymer resin (**Figure 1a**). Solving the inverse ultrasound DSA problem using existing theory enables computing the ultrasound transducer settings (amplitude and phase) to assemble almost any pattern of particles in an arbitrary-shaped fluid reservoir lined with any number of transducers.^[22] Here, we energize two ultrasound transducers that oppose each other (marked yellow in **Figure 1a**), and the acoustic radiation force associated with the ultrasound wave field drives the particles to the nodes of the standing ultrasound wave field,^[25,30] which results in a pattern of parallel lines of particles spaced a half-wavelength apart ($s = \lambda/2$) in the liquid photopolymer resin. A digital light processing projector exposes the liquid photopolymer resin to visible/ultraviolet (UV) light through the transparent reservoir floor, which causes the liquid photopolymer resin to cross-link and cure into a layer of thickness h_0 that fixates the pattern of particles in place^[31] (inset image in **Figure 1a**). The build plate lowers to $h_f > h_0$ above the transparent reservoir floor, and additional visible/UV light exposure cures the resin layer with thickness h_f to adhere it to the build plate (**Figure 1b**). The build plate lifts out of the reservoir (**Figure 1c**), and we replenish the particle/liquid photopolymer resin mixture to ensure a consistent weight fraction of particles in each resin layer. We repeat the process shown in **Figure 1a–c** to 3D print the engineered material layer-by-layer, and each layer contains a user-specified pattern of particles to enable tailoring the microstructure of the material (**Figure 1d**) (see video of the manufacturing process in the Supporting Information). Furthermore, we use the SLA process to control the macroscale geometry of the material.

3. Single-Layer Engineered Materials

To demonstrate the capability of the ultrasound DSA/SLA manufacturing process for fabricating macroscale user-specified patterns within each material layer, we fabricate $8.00 \times 5.00 \times 0.45$ mm single-layer material specimens containing line patterns of nickel-coated carbon fibers of length $l = 100$ μm and diameter $d = 10$ μm , and $9.00 \times 9.00 \times 0.45$ mm material specimens with complex user-specified patterns of nickel-coated carbon fibers. **Figure 2a** shows optical images of single-layer material specimens containing line patterns of aligned nickel-coated carbon fibers with half-wavelength

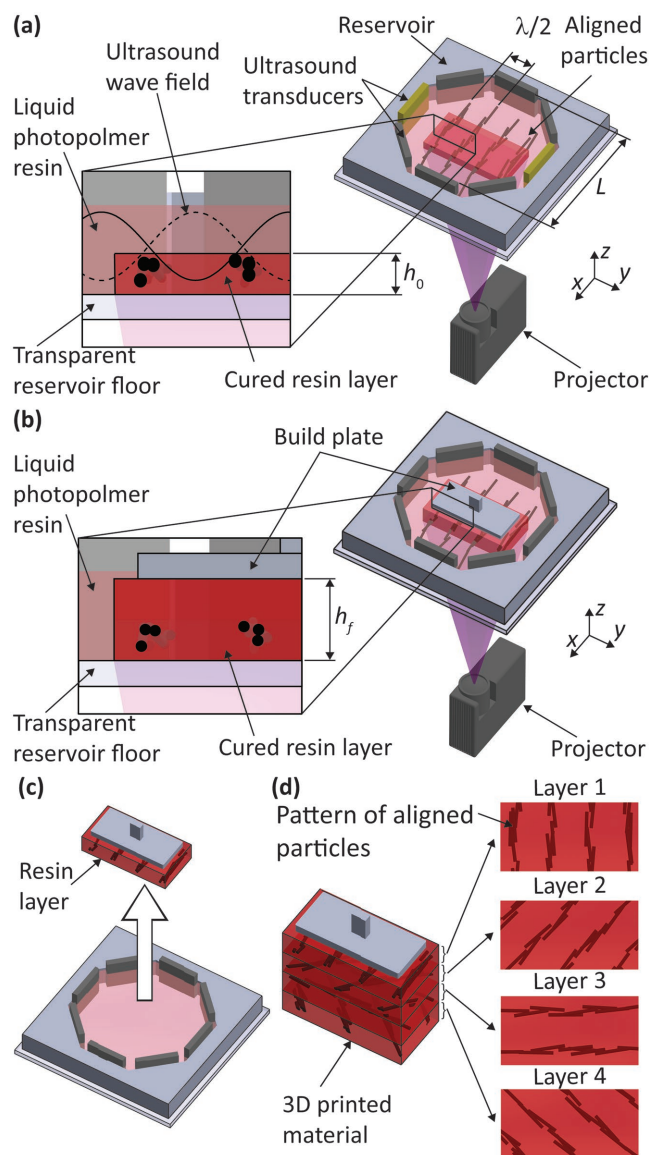


Figure 1. 3D printing materials with user-specified patterns of particles embedded in a matrix material. a) The process sequentially employs ultrasound directed self-assembly to organize a user-specified pattern of aligned particles in a thin layer of resin contained in a reservoir, and b) cures and c) lifts the layer of resin to d) fabricate materials layer-by-layer via stereolithography.

spacing $s = \lambda/2 = 0.45$ mm and user-specified orientation angle $\theta_d = 0^\circ, 45^\circ, 90^\circ$, and -45° , respectively. Inset images indicate the active pair of ultrasound transducers to organize each line pattern in yellow. We quantify the alignment of the nickel-coated carbon fibers in each material specimen shown in **Figure 2a** using the 2D fast Fourier transform (FFT) to measure anisotropy in each of the optical images^[32] (see the Experimental Section for details). **Figure 2b** shows the FFT anisotropy as a function of the angle θ , measured with reference to the vertical, for each of the material specimens shown in **Figure 2a** with $\theta_d = 0^\circ$ (red diamond marker), 45° (green square), 90° (yellow circle), and -45° (blue triangle). We quantify the angle at which the FFT is maximum and the full width

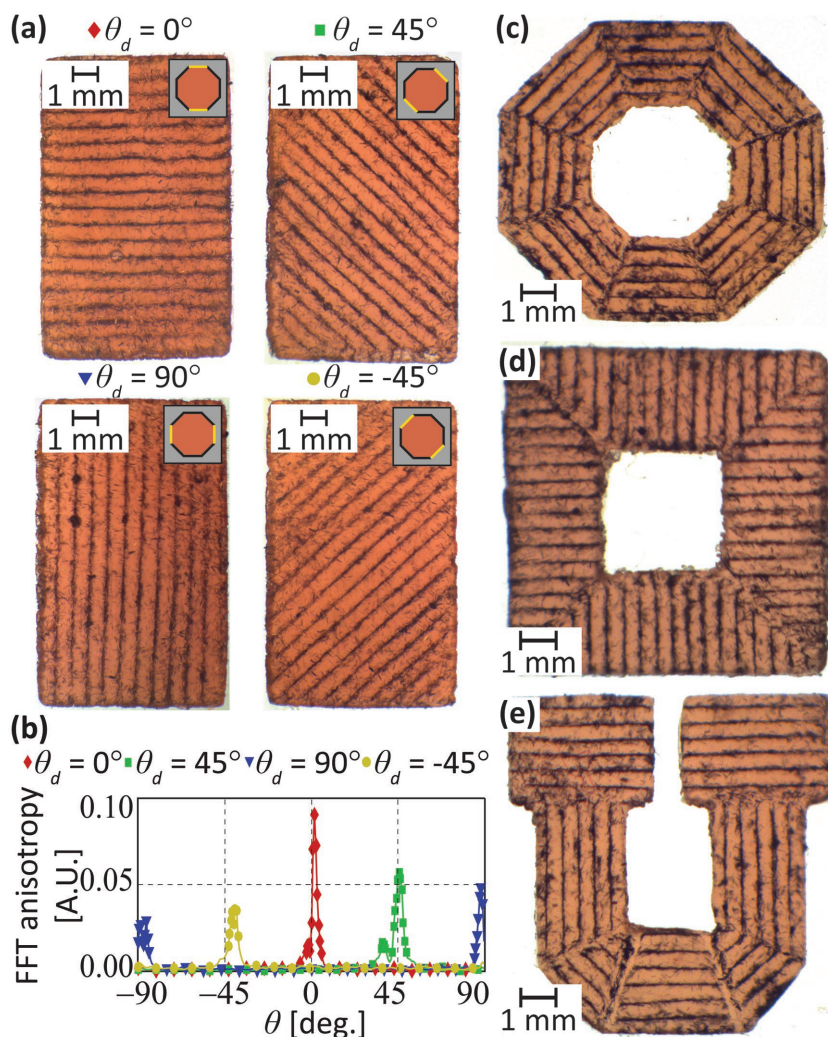


Figure 2. Single-layer material specimens with user-specified patterns of nickel-coated carbon fibers. a) Material specimens containing line patterns of aligned nickel-coated carbon fibers oriented in user-specified angles $\theta_d = 0^\circ$, 45° , 90° , and -45° . b) FFT anisotropy of each material specimen as a function of the image angle θ . Material specimens containing complex patterns of aligned nickel-coated carbon fibers organized into c) octagonal, d) square, e) the University of Utah “U-logo” configurations.

at half maximum of the FFT anisotropy distribution for each single-layer material specimen. The difference between the angle at which the FFT is maximum and the user-specified angle is 1.62° , 0.59° , 1.89° , and 5.54° for $\theta_d = 0^\circ$, 45° , 90° , and -45° , respectively, indicating excellent alignment of the line patterns of nickel-coated carbon fibers in the user-specified direction. The corresponding full width at half maximum, which indicates how well the individual nickel-coated carbon fibers are aligned with the angle at which the FFT is maximum, is 2.16° , 4.32° , 8.65° , and 5.05° , respectively, demonstrating good alignment. Figure 2a shows small regions with locally nonstraight lines and nonuniform concentrations of nickel-coated carbon fiber. These defects are due to near-field effects, acoustic streaming,^[33] and squeeze flow of the resin as the build plate is lowered into the reservoir (Figure 1b), which may displace the nickel-coated carbon fibers and disrupt the resulting patterns within each resin layer.

The spacing between pattern features $s = \lambda/2 = c_f/2f$ decreases with increasing frequency of the ultrasound wave field, where c_f is the sound propagation speed in the fluid medium. However, increasing the frequency also increases viscous attenuation, which reduces the magnitude of the acoustic radiation force that assembles the particles into an organized pattern and, thus, limits the minimum achievable pattern spacing.^[27]

In addition to simple line patterns, the ultrasound DSA/SLA manufacturing process enables organizing complex patterns of particles that cover macroscale areas. We accomplish this by fabricating the resin layer in multiple sections, where each section contains a line pattern of particles with a user-specified orientation angle θ_d . The sequence of curing sections does not affect the final pattern of particles. Figure 2c–e shows optical images of single-layer material specimens with nickel-coated carbon fibers organized into complex patterns, including a hollow octagon (Figure 2c), square (Figure 2d), and the University of Utah “U-logo” (Figure 2e).

In contrast with existing ultrasound DSA techniques based on phased arrays, which are limited to creating pattern features with nonsharp corners due to the ultrasound wave field interference patterns,^[22,23] the ultrasound DSA/SLA manufacturing process enables fabricating patterns of particles with sharp features by combining multiple material sections. Additionally, it is possible to organize patterns of particles with different weight fraction, material type, and/or geometry within each material section by exchanging the particle/liquid photopolymer resin mixture between material sections. Figure 2c–e shows small gaps ($<350 \mu\text{m}$) between some neighboring sections. These gaps are attributed to squeeze flow generated as the build plate is lowered during the manufacturing process (Figure 1b). They can be mitigated by using a photopolymer resin that adheres well to the transparent reservoir floor and, thus, reduces the displacement of the partially cured sections due to squeeze flow.

4. Multilayer Engineered Materials

To demonstrate the capability of the ultrasound DSA/SLA manufacturing process for fabricating multilayer materials, we fabricate macroscale specimens containing Bouligand structures, which are found in biological and composite laminate materials and are known to provide, e.g., enhanced mechanical strength and puncture resistance.^[34] Figure 3 shows four-layer specimens ($8.0 \times 5.0 \times 1.8 \text{ mm}$) with a Bouligand microstructure consisting of line patterns of nickel-coated carbon fibers

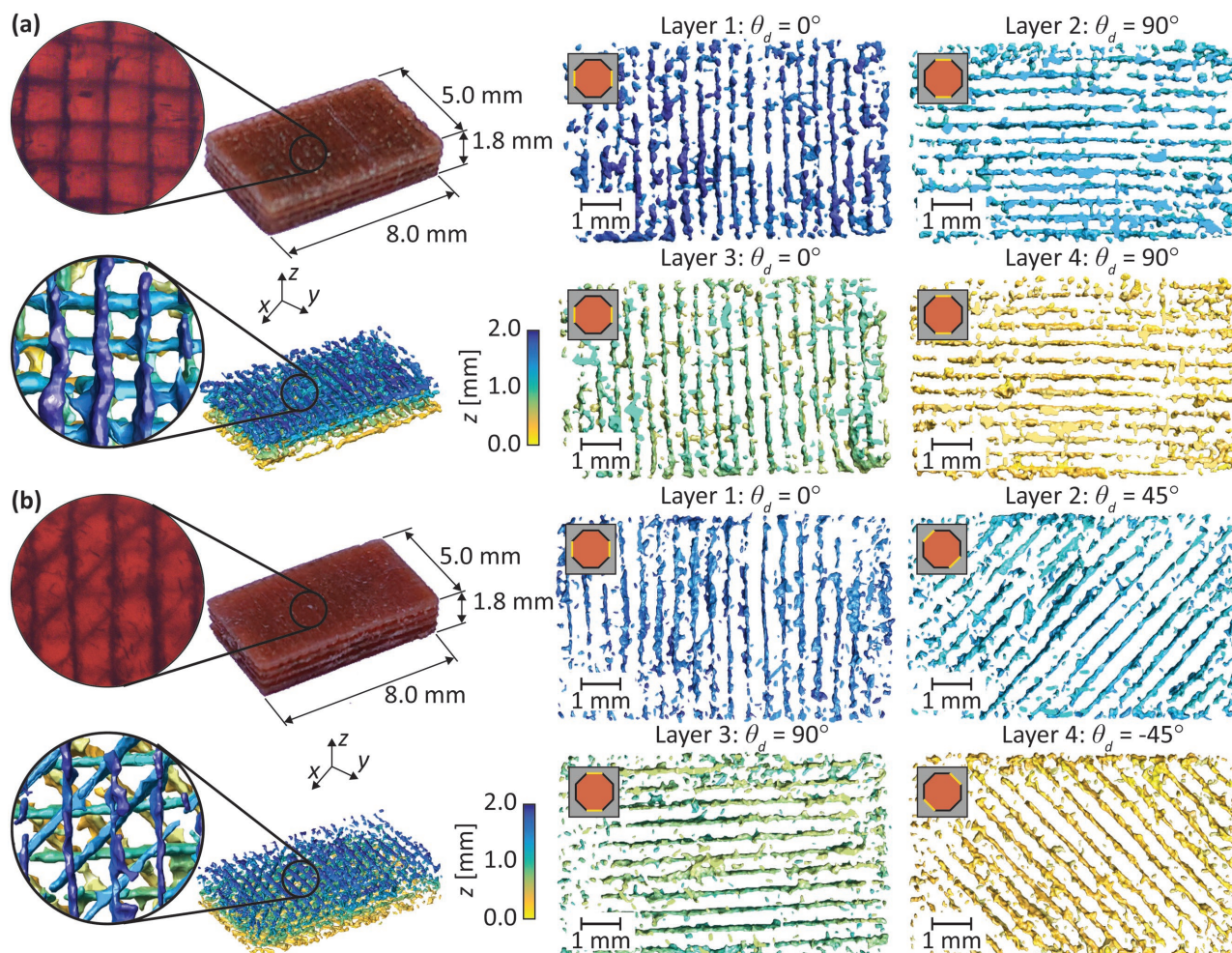


Figure 3. 3D printed multilayer material specimens containing Bouligand microstructures of aligned nickel-coated carbon fibers. a) Four-layer material specimen containing line patterns with θ_d of 0° , 90° , 0° , and 90° , in layers 1–4, respectively. b) Four-layer material specimen containing line patterns with user-specified alignment angles θ_d of 0° , 45° , 90° , and -45° , in layers 1–4, respectively. The energized transducers are marked in yellow in the inset figures.

aligned in user-specified orientations $\theta_d = 0^\circ$, 90° , 0° , and 90° (Figure 3a), and $\theta_d = 0^\circ$, 45° , 90° , and -45° (Figure 3b) in layers 1–4, respectively. Figure 3 shows trimetric views of the specimens imaged optically and via X-ray computed tomography (CT) (see the Experimental Section for details), and inset images show a top-view, where color represents the z -height in the specimen. Furthermore, Figure 3 shows a top-view of each individual layer, with inset images indicating the pair of ultrasound transducers energized to create the line pattern, in yellow. The “thickness” of the pattern features is dependent on the magnitude of the acoustic radiation force and the nickel-coated carbon fiber weight fraction and density. Increasing the magnitude of the acoustic radiation force decreases the spacing between the nickel-coated carbon fibers organized at the nodes of the ultrasound wave field, and results in “thinner” pattern features. Increasing the weight fraction and decreasing the density of the nickel-coated carbon fibers increases the number of nickel-coated carbon fibers that agglomerate at the nodes of the ultrasound standing wave, creating “thicker” pattern features. Also, increasing the nickel-coated carbon fiber density affects their

diffusive properties when dispersed in photopolymer. However, photopolymer viscosity and short ultrasound DSA process time cause diffusion to not significantly affect the resulting patterns. The minimum resin layer thickness h_f is constrained by the thickness of the pattern features in the z -direction (referring to Figure 3), and because the pattern features are contained within a single resin layer, no interaction between pattern features of adjacent resin layers occurs. From Figure 3, we observe small variations in thickness along each line of nickel-coated carbon fibers. These variations and imperfections occur for the same reasons discussed with single-layer material specimens. Limited resolution ($\geq 10 \times 10 \times 10 \mu\text{m}$ voxel size) of the X-ray CT imaging may also contribute to gaps between fibers or connected regions between lines in Figure 3.

5. Electrically Conductive Engineered Materials

To demonstrate the possibilities of this manufacturing technique in the context of engineered materials with embedded

functionality, we have fabricated a single-layer material specimen containing a line pattern of aligned nickel-coated carbon fibers, which form a percolated network and enable tailoring the electrical conductivity of the material. We place two electrical probes 1 mm apart at different locations along the lines of nickel-coated carbon fibers and between neighboring lines of nickel-coated carbon fibers to measure the “wire resistance” and “insulator resistance,” respectively, by applying direct-current voltage V to the electrical probes, measuring the resulting current I , and computing the resistance $R = V/I$ ^[9] (see the Experimental Section for details). We measure an average wire resistance of 59.7 Ω and insulation resistance of 112.7 M Ω , with a standard deviation of 14.5 Ω and 23.2 M Ω , respectively, showing that the lines of aligned nickel-coated carbon fibers are electrically conductive, yet insulated from each other. This example illustrates how the ultrasound DSA/SLA manufacturing process enables tailoring the conductivity of a material in specific directions, or 3D printing materials with embedded insulated electrical wiring or sensors, which finds application in engineering systems.

6. Discussion

The ultrasound DSA/SLA manufacturing process time is dependent on several factors including the ultrasound DSA process time required to organize a pattern of particles, the resin curing times, and the time required to replenish the particle/liquid photopolymer resin mixture after each layer or section is cured. The ultrasound DSA process time is a function of the acoustic radiation force that drives the particles to the nodes of the ultrasound wave field, and the drag force that resists any particle motion through the fluid medium.^[26,30] The magnitude of the acoustic radiation force is proportional to the volume of the particle ($\pi d^2 l/4$ for a cylindrical fiber of diameter d and length l), the frequency f , the squared amplitude of the ultrasound wave field, and the acoustic contrast factor Φ , which depends on the difference in density and compressibility between the particle and fluid medium.^[35,36] Alternatively, the amplitude of the drag force is proportional to the particle diameter d and length l and the viscosity of the particle/fluid medium mixture.^[35,37] We note that the viscosity of the particle/fluid medium mixture is known to increase with increasing weight fraction of nanoparticles.^[38] In the experiments documented in this work, we observe an ultrasound DSA process time of ≈ 1 s, which is significantly shorter than the process times required by DSA techniques based on electric and magnetic fields, typically on the order of tens of seconds.^[19,21] We then cure the layer of resin in two steps: the initial cure step, which fixates the pattern of particles in place (Figure 1a) and the final cure step, which adheres the resin layer to the build plate (Figure 2a). The curing time required for the initial (Figure 1a) and final curing steps (Figure 1b) depends on the photopolymer resin properties and the weight fraction of particles, and is inversely proportional to the intensity of the projected UV-visible light and proportional to the squared layer thicknesses h_0^2 and h_f^2 for the initial and final curing steps.^[39] For the specimens shown in this paper, the initial and final curing times are ≈ 7 and 11 s, respectively. In contrast to laser-based photocuring

processes, which require a laser to trace the cross-section of each resin layer, the projector-based process cures the entire resin layer at once and, thus, the curing time is independent of the x - and y -material dimensions.^[28,29] After each material layer is fabricated, we replenish the particle/liquid photopolymer resin mixture to ensure a consistent weight fraction and distribution of particles in each layer. In this work, we replenish the particle/liquid photopolymer resin mixture with a syringe, which requires ≈ 60 s, but can be reduced drastically by implementing an automated fluid dispenser.

Scalability of the ultrasound DSA/SLA manufacturing process is achieved by increasing the height of the ultrasound DSA/SLA apparatus in the z -direction and the reservoir size in the x - and y -directions (referring to Figure 1a). However, increasing the reservoir size increases the distance between the ultrasound transducers and, thus, the ultrasound wave propagation distance, which increases viscous attenuation of the ultrasound wave field and, in turn, reduces the magnitude of the acoustic radiation force available to assemble the particles into the desired pattern.^[27] As a result, increasing the reservoir size increases the ultrasound DSA process time required to organize a pattern of particles. Viscous attenuation is counteracted by increasing the acoustic radiation force magnitude, by increasing the particle dimensions, the ultrasound wave field amplitude, and acoustic contrast factor Φ , or decreasing the ultrasound wave field frequency and the viscosity of the fluid medium.

7. Conclusions

In conclusion, we have demonstrated, for the first time, a manufacturing process that integrates ultrasound DSA and SLA to 3D print multilayer engineered materials with arbitrary macroscale geometry and user-specified microstructure based on a pattern of particles embedded in a polymer matrix. We have illustrated the capability of the manufacturing process by 3D printing engineered materials containing a user-specified Bouligand microstructure and engineered materials with electrically conductive lines of nickel-coated carbon fibers. In contrast with existing manufacturing techniques, the ultrasound DSA/SLA manufacturing process enables fabricating engineered materials with both macroscale complex 3D geometries and user-specified microstructure. Thus, the ultrasound DSA/SLA manufacturing process bridges the gap between engineered materials with unique physical properties demonstrated in a laboratory setting and macroscale engineering applications. This manufacturing process enables implementing material designs for a broad range of applications including multifunctional composite materials, acoustic and electromagnetic cloaking, and subwavelength imaging.

8. Experimental Section

Ultrasound DSA/SLA Apparatus: The ultrasound DSA/SLA apparatus comprises a kit-based SLA device (mUVe 1.1 DLP), which was modified by attaching an octagonal reservoir lined with eight ultrasound transducers (PZT type SM112, center frequency $f = 1.65$ MHz) to the transparent reservoir floor (Figure S1, Supporting Information).

To generate a standing ultrasound wave field, a pair of ultrasound transducers was energized that oppose each other, with a sinusoidal voltage of amplitude $V_0 = 25 V_{\text{RMS}}$ and frequency $f = 1.65$ MHz using a signal generator (Tektronix AFG3102) and radio-frequency amplifier (ENI A150).

Single- and Multilayer Material Specimen Fabrication: The single- and multilayer material specimens shown in Figures 2 and 3 consist of 1.0 weight percent of nickel-coated carbon fibers (Conductive Composites Company, Heber, UT) of length $l = 100$ μm and diameter $d = 10$ μm , dispersed in a liquid photopolymer resin (Maker Juice G+) with viscosity 12 cP via tip sonication (Hielscher UP200Ht) for 15 min at 15 W.

Conductive Material Specimen Preparation and Electrical Resistance Characterization: The electrically conductive material specimens (dimensions $5.00 \times 5.00 \times 0.35$ mm), contain 2.0 weight percent nickel-coated carbon fibers (Conductive Composites Company, Heber, UT) of length $l = 100$ μm and diameter $d = 10$ μm dispersed in a liquid photopolymer resin (Maker Juice G+) with viscosity 12 cP via tip sonication (Hielscher UP200Ht) for 15 min at 15 W. The manufacturing process shown in Figure 1a was followed to create a pattern of aligned nickel-coated carbon fibers via ultrasound DSA and then the liquid photopolymer resin was exposed to visible/UV light (mean wavelength 365 nm) for 8 s to polymerize the resin and fixate the pattern of nickel-coated carbon fibers in place. The final step shown in Figure 1b–d was omitted to ensure that the line pattern of nickel-coated carbon fibers is not fully enclosed in the resin, which would inhibit measurement of electrical resistance. To measure the electrical resistance of the conductive material specimen, a two-probe setup was used, where the probes are placed 1 mm apart along (1) a single line of nickel-coated carbon fibers to measure the “wire resistance,” and (2) on two neighboring lines of nickel-coated carbon fibers to measure the “insulator resistance” (Figure S2a–c, Supporting Information). A parameter analyzer (Keithley 4200) was used to apply a voltage sweep from -10 to 10 V, in 0.5 V increments, and the resulting electrical current flowing between the probes was measured. The resistance was calculated as the slope of the line that best fits the voltage–current data, which is calculated using least-squares linear regression (Figure S2d, Supporting Information). The current amplitude was limited to ≤ 100 mA to avoid damaging the parameter analyzer and, thus, all data points for which the current measurement saturates at 100 mA were removed to avoid spurious resistance values. The electrical resistance measurements were repeated on a representative sample of seven lines of nickel-coated carbon fibers near the center of the material specimen to calculate the mean and standard deviation of the wire and insulator resistances (Figure S2e,f, Supporting Information). It was observed that the voltage–current data were not perfectly linear, and exhibited trends similar to that of a transient voltage suppression diode.^[40] This was likely caused by a thin coating of resin forming around the nickel-coated carbon fibers, which impedes current flow until the applied voltage exceeds the dielectric breakdown strength of the resin coating.^[41] (MATLAB code and data available upon request).

Optical Imaging: The material specimens shown in Figures 2 and 3 were imaged using a digital camera (AmScope MT500) with 5.0 MP resolution and magnification of $1.0\times$ (Figures 2a and 3 and Figure S2e (Supporting Information)) and $0.5\times$ (Figure 2c–g). For each material specimen, multiple images were captured at different focal depths and then merged into a single image to ensure clarity.

X-Ray Computed Tomography: To image the Bouligand structures shown in Figure 3, X-ray CT (Varian BIR 150/130) was first used to produce a 3D grayscale model of the material specimen, with lighter voxels representing nickel-coated carbon fibers and darker voxels representing resin. The 3D grayscale model was thresholded to remove voxels with values below 30.0% of the maximum voxel intensity in the 3D grayscale model to ensure that the thickness of the lines of nickel-coated carbon fibers in the X-ray CT images match those of the optical images. Finally, iso-surfaces were generated around regions of connected voxels to create the X-ray CT images shown in Figure 3 (MATLAB code and data available upon request).

Fast Fourier Transform Anisotropy Quantification: To compute the FFT anisotropy for the material specimens shown in Figure 2a, the images were cropped to the 4.5×4.5 mm region in the center of the image to remove edge effects (Figure S3a, Supporting Information) and the 2D FFT of the image (Figure S3b, Supporting Information) was computed. A circular projection was performed, wherein the squared absolute values of the 2D FFT were summed radially from the center of the 2D FFT in each direction to calculate the FFT anisotropy as a function of θ , and the FFT anisotropy was normalized so that the integral over $-\pi/2 \leq \theta \leq \pi/2$ had unit magnitude (Figure S3c, Supporting Information) (MATLAB code and data available upon request).

Supporting Information

Supporting Information is available from the Wiley Online Library or from the author.

Acknowledgements

The authors acknowledge support from the Army Research Office under contract No. W911NF-16-1-0457, and J.G. acknowledges support from a NASA Space Technology Research Fellowship, award No. NNX15AP30H. The authors acknowledge access to X-Ray computed tomography through the University of Utah Composite Mechanics Laboratory, directed by Prof. Michael Czubaj. The authors thank Dr. Mia Siochi and Dr. Godfrey Sauti from NASA Langley for fruitful discussions.

Conflict of Interest

The authors declare no conflict of interest.

Keywords

3D printing, engineered materials, ultrasound directed self-assembly

Received: May 10, 2017

Revised: June 12, 2017

Published online:

- [1] Z. G. Nicolaou, A. E. Motter, *Nat. Mater.* **2012**, *11*, 608.
- [2] M. H. Al-Saleh, U. Sundararaj, *Carbon* **2009**, *47*, 2.
- [3] S. J. Corbitt, M. Francoeur, B. Raeymaekers, *J. Quant. Spectrosc. Radiat. Transfer* **2015**, *158*, 3.
- [4] S. A. Cummer, J. Christensen, A. Alù, *Nat. Rev. Mater.* **2016**, *1*.
- [5] V. M. Shalaev, *Nat. Photonics* **2007**, *1*, 41.
- [6] D. Schurig, J. J. Mock, B. J. Justice, S. A. Cummer, J. B. Pendry, A. F. Starr, D. R. Smith, *Science* **2006**, *314*, 974.
- [7] S. Zhang, L. Yin, N. Fang, *Phys. Rev. Lett.* **2009**, *102*, 194301.
- [8] X. Zhang, Z. Liu, *Nat. Mater.* **2008**, *7*, 435.
- [9] W. Guo, C. Liu, X. Sun, Z. Yang, H. G. Kia, H. Peng, *J. Mater. Chem.* **2012**, *22*, 903.
- [10] C. Enkrich, F. Pérez-Willard, D. Gerthsen, J. F. Zhou, T. Koschny, C. M. Soukoulis, M. Wegener, S. Linden, *Adv. Mater.* **2005**, *17*, 2547.
- [11] N. Feth, C. Enkrich, M. Wegener, S. Linden, *Opt. Express* **2007**, *15*, 501.
- [12] H. Schift, *J. Vac. Sci. Technol., B Microelectron. Nanometer Struct.* **2008**, *26*, 458.
- [13] F. Zhou, W. Cao, B. Dong, T. Reissman, W. Zhang, C. Sun, *Adv. Opt. Mater.* **2016**, *4*, 1034.

- [14] T. D. Clark, R. Ferrigno, J. Tien, K. E. Paul, G. M. Whitesides, *J. Am. Chem. Soc.* **2002**, 124, 5419.
- [15] S. B. Darling, *Prog. Polym. Sci.* **2007**, 32, 1152.
- [16] M. Grzelczak, J. Vermant, E. M. Furst, L. M. Liz-Marzán, *ACS Nano* **2010**, 4, 3591.
- [17] Y. Chen, H. Liu, T. Ye, J. Kim, C. Mao, *J. Am. Chem. Soc.* **2007**, 129, 8696.
- [18] P. V. Kamat, K. G. Thomas, S. Barazzouk, G. Girishkumar, K. Vinodgopal, D. Meisel, *J. Am. Chem. Soc.* **2004**, 126, 10757.
- [19] Y. Yang, Z. Chen, X. Song, Z. Zhang, J. Zhang, K. K. Shung, Q. Zhou, Y. Chen, *Adv. Mater.* **2017**, 29, 1605750.
- [20] J. H. Promislow, A. P. Gast, *Langmuir* **1996**, 12, 4095.
- [21] J. J. Martin, B. E. Fiore, R. M. Erb, *Nat. Commun.* **2015**, 6, 8641.
- [22] J. Greenhall, F. Guevara Vasquez, B. Raeymaekers, *Appl. Phys. Lett.* **2016**, 108, 103103.
- [23] M. Prisbrey, J. Greenhall, F. Guevara Vasquez, B. Raeymaekers, *J. Appl. Phys.* **2017**, 121, 014302.
- [24] J. Greenhall, F. Guevara Vasquez, B. Raeymaekers, *Appl. Phys. Lett.* **2013**, 103, 074103.
- [25] L. P. Gor'kov, *Phys.-Dokl.* **1962**, 6, 773.
- [26] R. R. Collino, T. R. Ray, R. C. Fleming, C. H. Sasaki, H. Haj-Hariri, M. R. Begley, *Extreme Mech. Lett.* **2015**, 5, 37.
- [27] L. E. Kinsler, A. R. Frey, A. B. Coppens, J. V. Sanders, *Fundamentals of Acoustics*, 4th ed., John Wiley, New York **2000**.
- [28] M.-S. Scholz, B. W. Drinkwater, R. S. Trask, *Ultrasonics* **2014**, 54, 1015.
- [29] T. M. Llewellyn-Jones, B. W. Drinkwater, R. S. Trask, *Smart Mater. Struct.* **2016**, 25, 02LT01.
- [30] J. Greenhall, F. Guevara Vasquez, B. Raeymaekers, *Appl. Phys. Lett.* **2014**, 105, 144105.
- [31] J. V. Crivello, E. Reichmanis, *Chem. Mater.* **2014**, 26, 533.
- [32] C. E. Ayres, B. Shekhar Jha, H. Meredith, J. R. Bowman, G. L. Bowlin, S. C. Henderson, D. G. Simpson, *J. Biomater. Sci., Polym. Ed.* **2008**, 19, 603.
- [33] A. L. Bernassau, P. Glynne-Jones, F. Gesellchen, M. Riehle, M. Hill, D. R. S. Cumming, *Ultrasonics* **2014**, 54, 268.
- [34] S. E. Naleway, M. M. Porter, J. McKittrick, M. A. Meyers, *Adv. Mater.* **2015**, 27, 5455.
- [35] S. Yamahira, S. Hatanaka, M. Kuwabara, S. Asai, *Jpn. J. Appl. Phys.* **2000**, 39, 3683.
- [36] J. J. Faran, *J. Acoust. Soc. Am.* **1951**, 23, 405.
- [37] P. J. Westervelt, *J. Acoust. Soc. Am.* **1951**, 23, 312.
- [38] P. Pötschke, T. D. Fornes, D. R. Paul, *Polymer* **2002**, 43, 3247.
- [39] J. H. Lee, R. K. Prud'Homme, I. A. Aksay, *J. Mater. Res.* **2001**, 16, 3536.
- [40] M. Bley, M. F. Filho, A. Raizer, *IEEE Potentials* **2004**, 23, 43.
- [41] L. A. Dissado, J. C. Fothergil, in *Electrical Degradation and Breakdown in Polymers*, Vol. 9, EIT, London, United Kingdom **1992**, pp. 271–286.